

Alma Mater Studiorum Università di Bologna
Archivio istituzionale della ricerca

A Computational-Effective Field-Oriented Control Strategy for Accurate and Efficient Electric Propulsion of Unmanned Aerial Vehicles

This is the final peer-reviewed author's accepted manuscript (postprint) of the following publication:

Published Version:

Bosso, A., Conficoni, C., Raggini, D., Tilli, A. (2021). A Computational-Effective Field-Oriented Control Strategy for Accurate and Efficient Electric Propulsion of Unmanned Aerial Vehicles. IEEE/ASME TRANSACTIONS ON MECHATRONICS, 26(3), 1501-1511 [10.1109/TMECH.2020.3022379].

Availability:

This version is available at: <https://hdl.handle.net/11585/806492> since: 2021-02-25

Published:

DOI: <http://doi.org/10.1109/TMECH.2020.3022379>

Terms of use:

Some rights reserved. The terms and conditions for the reuse of this version of the manuscript are specified in the publishing policy. For all terms of use and more information see the publisher's website.

This item was downloaded from IRIS Università di Bologna (<https://cris.unibo.it/>).
When citing, please refer to the published version.

(Article begins on next page)

This is the final peer-reviewed accepted manuscript of:

A. Bosso, C. Conficoni, D. Raggini and A. Tilli, "A Computational-Effective Field-Oriented Control Strategy for Accurate and Efficient Electric Propulsion of Unmanned Aerial Vehicles," in *IEEE/ASME Transactions on Mechatronics*, vol. 26, no. 3, pp. 1501-1511, June 2021

The final published version is available online at:

<https://doi.org/10.1109/TMECH.2020.3022379>

Terms of use:

Some rights reserved. The terms and conditions for the reuse of this version of the manuscript are specified in the publishing policy. For all terms of use and more information see the publisher's website.

This item was downloaded from IRIS Università di Bologna (<https://cris.unibo.it/>)

When citing, please refer to the published version.

A Computational-Effective Field-Oriented Control Strategy for Accurate and Efficient Electric Propulsion of Unmanned Aerial Vehicles

Alessandro Bosso, *Member, IEEE*, Christian Conficoni, Davide Raggini, Andrea Tilli

Abstract—In this work, we introduce an easy-to-implement sensorless controller specifically designed for the regulation of the propellers of Unmanned Aerial Vehicles (UAVs). As motivation, we present a comparison of the usual motor control architectures, i.e., Field-Oriented Control (FOC) and Brushless DC (BLDC) control, with special attention to the typical back-ElectroMotive Force (back-EMF) shapes found in this application. In particular, we show that the adoption of sensorless FOC provides several advantages, both from the efficiency and the signal quality viewpoints, provided that accurate rotor position reconstruction is available. Therefore, a recently proposed observer is integrated into a nested FOC architecture, with formal stability guarantees and low computational effort, making the resulting strategy suitable for implementation in embedded computing systems. The algorithm is then compared experimentally to a sensorless BLDC controller and a high-end commercial drive, thus validating the previous results and showing effective time-varying speed tracking, as required for precise aggressive maneuvering. These features of efficiency, accuracy, and simplicity might prove instrumental in bolstering the introduction of a novel class of high-performance, robust UAV sensorless controllers in the forthcoming years.

Index Terms—Aircraft propulsion, energy efficiency, motor drives, sensorless control, Unmanned Aerial Vehicles.

I. INTRODUCTION

ELECTRICALLY powered Unmanned Aerial Vehicles (UAVs) are becoming an ever-growing source of interest for civil, military, and industrial applications [1], [2]. On this topic, several works from different communities can be found [3], and a significant effort has been dedicated to improving the related technology, control accuracy, and effectiveness in numerous demanding scenarios. A crucial UAV design issue is flight endurance, typically assessed in the literature at the flight control level, e.g., considering trajectory optimization to minimize energy losses [4], [5]. Alternative power sources [6], on purpose design [7], and energy harvesting systems [8] have also been explored to enhance this feature. However, not only flight endurance but also tracking performance is critically affected by the propeller drives, since maneuvering is achieved by regulating the propeller speed/thrust [9].

In this respect, our work is focused on the control of multirotor UAV electric motors, addressing its impact on efficiency and accuracy. Notably, these features are related to the

electromagnetic structure of the motors, commonly permanent magnet machines. The typical driving technique for UAV propellers is sensorless Brushless DC (BLDC) control [10], [11], which is very popular nowadays because of its parameter-free implementation and simple position/speed reconstruction algorithms. We refer to [12], [13] for other techniques and their relation to UAV dynamic performance. Sensorless BLDC control is adequate if the motor back-ElectroMotive Force (back-EMF) has a trapezoidal shape. However, it is suboptimal in efficiency and accuracy whenever applied to other structures, in particular sinusoidal machines, known as Permanent Magnet Synchronous Machines (PMSMs). Instead, the optimal control technique for PMSMs, Field-Oriented Control (FOC), requires in general sophisticated sensorless algorithms and (at least partial) knowledge of the motor/load parameters. On the other hand, it theoretically guarantees the highest torque-per-current ratio and lowest torque distortion.

The objective of this paper is to propose a systematic strategy to enhance UAV actuator performance. Firstly, we analyze the back-EMF of UAV propeller motors and, noting that the shape is close to sinusoidal, we present an efficiency-accuracy comparative study of BLDC control and FOC applied to PMSMs. This analysis represents an extension of the one in [14], and we refer to [15] for a closely-related work. Afterward, we propose a simple yet theoretically-solid sensorless FOC controller. One crucial aim of this scheme is to reduce the need for a priori knowledge of the model while guaranteeing accurate position reconstruction, which is critical in preserving the FOC's desirable features during sensorless operation. In particular, a recent sensorless observer [16] is employed to increase the performance in variable-speed scenarios, without requiring any information of the mechanical dynamics and their parameters. The control scheme is then analyzed both from the theoretical and implementation perspective, featuring robust stability and a relatively low computational complexity. In view of these properties, the proposed strategy is particularly suitable for embedded computing systems, and it can be adapted without effort to different loads and operating conditions. Finally, the solution's effectiveness is confirmed in experimental tests, where a high-performance commercial sensorless FOC is used as a benchmark for comparison.

The article is organized as follows. In Section II, we study the experimental back-EMF of a set of small/medium size UAV propeller motors, highlighting their sinusoidal shape. Section III is devoted to a numerical comparison of BLDC control and FOC applied to PMSMs, showing the mechanical

A. Bosso, C. Conficoni, D. Raggini, and A. Tilli are with the Department of Electrical, Electronic and Information Engineering (DEI), University of Bologna, Viale Risorgimento, 2, 40136 Bologna, Italy. Email:{alessandro.bosso3, christian.conficoni3, davide.raggini2, andrea.tilli}@unibo.it

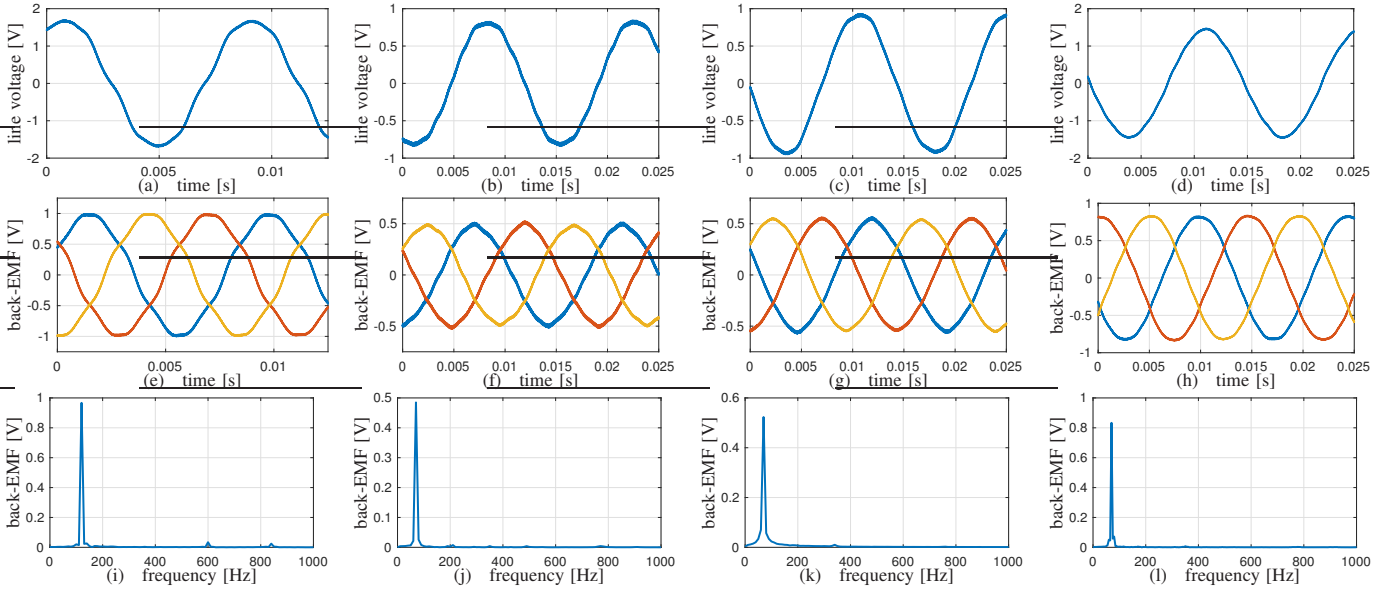


Fig. 1: Experimental results for back-EMF signal identification of UAV propeller motors dragged at constant speed. Plots (a)-(b)-(c)-(d) show one line-to-line voltage waveform of the four machines under test, plots (e)-(f)-(g)-(h) show the back-EMFs computed from two line-to-line voltages, while the back-EMF magnitude spectra (relative to the phase in blue) are reported in the third row, plots (i)-(j)-(k)-(l). Columns from left to right are related, respectively, to T-Motor Antigravity-4006-KV380, T-Motor MT2212-16-KV750, T-Motor U3-KV700 and a custom motor designed for small/medium-size UAVs [14].

operating conditions that suffer the most from a suboptimal driving choice. In Sections IV-V, the proposed sensorless FOC is introduced and experimentally tested, while Section VI draws some conclusive remarks and future research directions.

II. PROPELLER MOTORS ARE CLOSE TO SINUSOIDAL

Typically, permanent magnet brushless machines are roughly classified on the basis of the ideal shape of the back-EMF, leading to two main categories: Brushless-DC machines in case the shape is trapezoidal, and PMSMs if it is sinusoidal. This sharp separation does not account for the actual design of electric machines, as much as the technological limitations of the constructive process. As a consequence, even though the back-EMF should match the corresponding ideal shapes as well as possible, this feature is not reflected in practice, with trapezoidal waveforms resulting more intricate to achieve in comparison to the sinusoidal ones [17]. Following the experimental analysis undertaken in [14], we compare the back-EMF waveforms of four motors obtained by acquiring the line-to-line voltage of those motors, kept in open-circuit and dragged at a constant speed by an external machine. The experimental data are provided in Figure 1 in three different forms: one of the line-to-line voltages, the three back-EMFs relative to the neutral point (computed as $u_{iN} = (v_{ij} + v_{ik})/3$, with $i \in \{a, b, c\}$ and $j, k \in \{a, b, c\} \setminus \{i\}, j \neq k$, where v_{ij} are the line voltages), and the back-EMF magnitude spectrum. From these waveforms, it is highlighted how the motors, with different degrees of precision, resemble a sinusoidal shape.

III. BLDC CONTROL VS. FOC: ALGORITHMS AND PERFORMANCE

We now develop the analysis, considering PMSMs (i.e., pure sinusoidal back-EMF) for the mathematical modeling of the

motor. The deviation of the real machines from a sinusoidal shape is then inherently included in the experiments. Besides, the driving techniques comparison is performed under full knowledge of rotor position and speed, so that the ensuing results represent the best theoretical performance (no negative effect introduced by sensorless operation).

A. The UAV Actuator Model

The dynamics of PMSMs can be described, under some simplifying assumptions (balanced operating conditions, no magnetic saturation, and no iron losses), as follows [18]:

$$\begin{aligned} \dot{\lambda}_j &= u_j - Ri_j & j \in \{a, b, c\}, & \quad \dot{\vartheta} = \omega \\ \lambda_j &= \varphi_j(\vartheta) + Li_j \end{aligned} \quad (1)$$

where λ_j are the stator fluxes, u_j , i_j are the phase voltages (relative to the neutral point) and currents, respectively, φ_j are the rotor fluxes, ϑ is the rotor electrical position and ω is the electrical angular speed, while R , L are the stator resistance and inductance. In addition, the rotor fluxes can be expressed as $\varphi_a = \varphi_e \cos(\vartheta)$, $\varphi_b = \varphi_e \cos(\vartheta - 2\pi/3)$, $\varphi_c = \varphi_e \cos(\vartheta + 2\pi/3)$, with φ_e the nominal rotor flux amplitude. Employing standard computations involving amplitude-preserving Clarke and Park transformations, the current dynamics can be expressed in a generic rotating two-phase reference frame ϑ_r , such that $\dot{\vartheta}_r = \omega_r$, as follows:

$$\begin{aligned} \frac{d}{dt} i_d &= -\frac{R}{L} i_d + \frac{\omega \varphi_e}{L} \sin(\vartheta - \vartheta_r) + \omega_r i_q + \frac{u_d}{L} \\ \frac{d}{dt} i_q &= -\frac{R}{L} i_q - \frac{\omega \varphi_e}{L} \cos(\vartheta - \vartheta_r) - \omega_r i_d + \frac{u_q}{L}. \end{aligned} \quad (2)$$

Selecting $\vartheta = \vartheta_r$ yields the typical rotor-aligned frame used for sensed FOC. We complete the model by introducing the

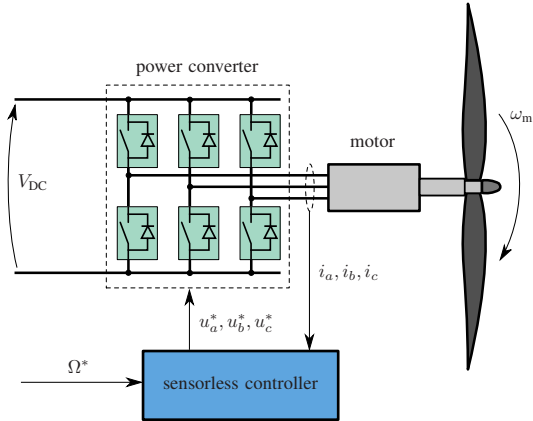


Fig. 2: UAV actuator scheme, with motor, propeller, power converter, controller, and some relevant signals. In particular, u_a^* , u_b^* , u_c^* denote the voltage commands before PWM modulation, V_{DC} is the power converter DC-link voltage, while Ω^* is a speed reference, e.g., imposed by a flight controller.

dynamics of the mechanical angular speed, $\omega_m = \omega/p$ (p are the motor pole pairs), including the electric torque and the propeller load, approximated for simplicity as:

$$\begin{aligned} J\dot{\omega}_m &= T_e - c_1\omega_m - c_2|\omega_m|\omega_m \\ T_e &= \frac{3}{2}p\varphi_e (i_q \cos(\vartheta - \vartheta_r) - i_d \sin(\vartheta - \vartheta_r)), \end{aligned} \quad (3)$$

where J is the total motor and load inertia, while c_1 and c_2 are positive load coefficients, related to the motor friction and the propeller aerodynamic torque. The complete structure of a UAV actuator, including the power converter and the controller, is summarized in Figure 2.

B. BLDC Control vs. FOC: Algorithms

One of the most popular control strategies for UAV motors is sensorless BLDC control. The core principle of BLDC control is to inject currents in two phases at a time, with their selection aimed at producing the maximum average torque. For the implementation of this technique, the values of the electrical angle ϑ are divided into six intervals (sextants). In each sextant, one leg of the power converter is driven with PWM at a specific duty-cycle, another is kept at fixed voltage (typically low¹), while the third is uncontrolled. This way, current flow is enabled between the two controlled phases. Sensorless BLDC control is typically based on Zero-Crossing algorithms, which keep track of the open phase voltage (embedding back-EMF information) to compute the sextant commutation instants in a parameter-free manner. A speed controller is then employed to assign the duty-cycle of the PWM-controlled phase. In fact, since the Zero-Crossing algorithms keep the current vector (on average) aligned with the back-EMF, it is possible to establish a relationship between the controlled phase duty-cycle and the rotating speed.

FOC techniques, on the other hand, aim to achieve the maximum torque-per-current ratio controlling the currents in

¹This is a widespread modulation strategy that has been shown to minimize converter switching power losses [19], [20].

TABLE I: T-Motor Antigravity-4006-KV380 parameters

Stator resistance R [m Ω]	108	Stator inductance L [μ H]	30.6
Number of pole pairs p	12	Rotor magnetic flux φ_e [mWb]	1.3

the synchronous frame (2), with $\vartheta_r = \vartheta$, so that $(i_d, i_q) \rightarrow (0, i_q^*)$, $i_q^* = 2T^*/(3p\varphi_e)$, where T^* is the requested torque. The typical FOC implementation scheme consists of nested PI controllers for current and speed loops [21], along with back-EMF compensation feedforward actions. In the context of sensorless control, the unmeasurable states are usually provided by nonlinear observers [22], [23]. As a consequence, FOC requires (at least partial) knowledge of the parameters for implementation, while BLDC control does not. In particular, either a priori parameter knowledge or identification schemes are needed. These considerations indicate that FOC generally requires more computational resources in a digital controller.

C. Efficiency and Accuracy of the Driving Techniques

Coherently with the experimental tests, we perform the analysis employing the parameters of T-Motor Antigravity-4006-KV380, which were experimentally estimated and are reported in Table I. To make the results independent of the specific mechanical load, we evaluate power and efficiency in 2-dimensional maps, depending on (constant) speed and the average torque resulting from the driving technique. In [14], a similar comparison was performed with some simplifying assumptions on the stator current during BLDC control operation, as it was supposed directly regulated with the PWM duty-cycle. Since we assumed constant current at each sextant except during the commutation transients, it was possible to directly compare the resistive power losses for a given average electric torque T_{avg} . In particular, assuming stepwise current response of the BLDC control after a sextant commutation:

$$P_{Cu, BLDC} = 2R \left(\frac{\pi T_{avg}}{3\sqrt{3}p\varphi_e} \right)^2, \quad P_{Cu, FOC} = \frac{3R}{2} \left(\frac{2T_{avg}}{3p\varphi_e} \right)^2, \quad (4)$$

which yields the ratio $P_{Cu, BLDC}/P_{Cu, FOC} = \pi^2/9$. This result implies that the BLDC control resistive losses are almost 10% higher than FOC losses. In [14], transient losses and power converter non-ideal components were accounted for as well, indicating the mechanical operating points where the adoption of FOC is particularly beneficial.

In practice, BLDC control is usually not implemented with a current control loop, thus only requesting specific duty-cycle values to run at the target speed, similarly to V/f open-loop strategies and in a parameter-free operation fashion. As a consequence, a theoretical analysis of BLDC control becomes more complicated than in the previous work. A viable strategy is, in principle, to consider the current at its steady-state, but the time-scale separation between the current dynamics and the sextant commutation is not satisfactory in the considered operative range. Therefore, BLDC control and FOC techniques have been tested on Matlab-Simulink[©], collecting the absorbed powers and the torque ripple. The simulator was designed with SimScape Power Systems to reproduce a realistic behavior of the power converter, and opportune PWM techniques (with carrier frequency at 15kHz)

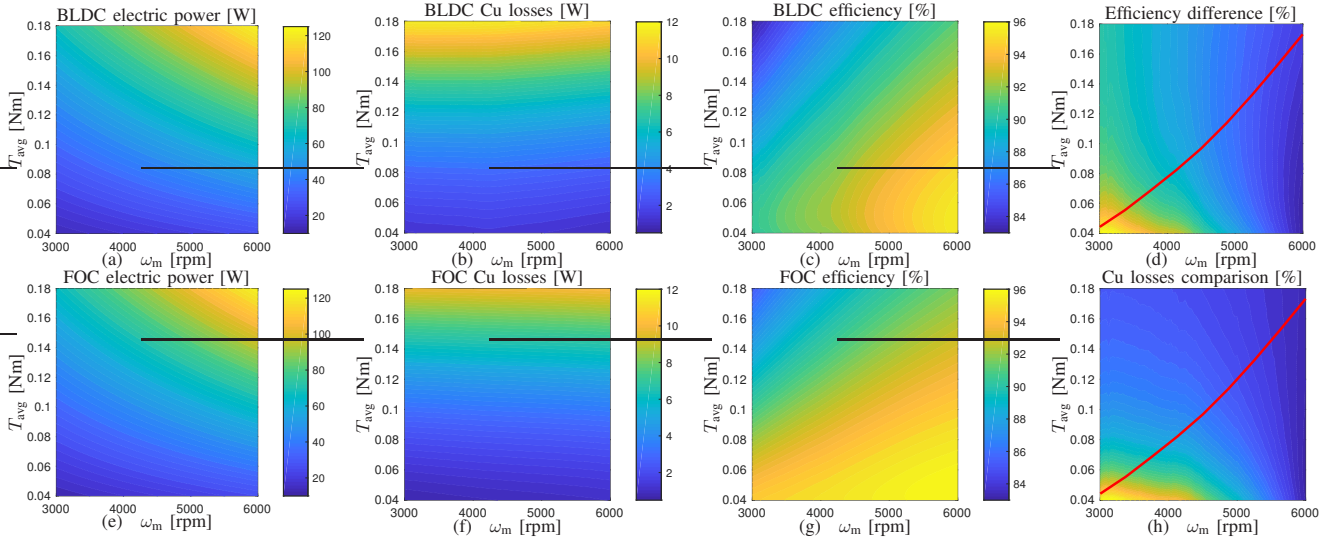


Fig. 3: Simulated power and efficiency of BLDC control and FOC, with respect to speed and the average generated torque. (a)-(e): average motor total power of BLDC control (top) and FOC (bottom), respectively. (b)-(f): resistive average power losses of BLDC control (top) and FOC (bottom). (c)-(g): average efficiency computed from total motor power and resistive power, for BLDC control (top) and FOC (bottom). (d): difference between FOC and BLDC control motor efficiencies. (h): difference of resistive losses of BLDC control and FOC, relative to FOC losses (percentage values). Note that the simulations yield higher values than the theoretical 10% of [14]. The experimental load curve of the propeller under test is reported in red.

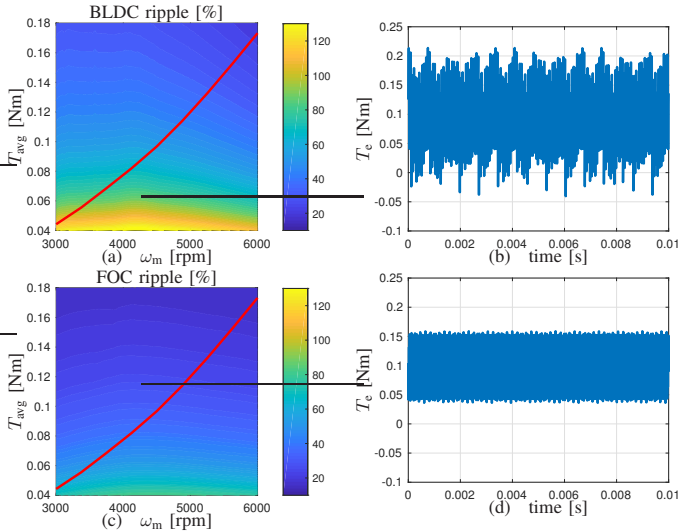


Fig. 4: Simulated torque ripple of BLDC control and FOC. (a)-(c): 2D maps of the torque ripple (percentage value), for BLDC control (top) and FOC (bottom). The experimental load curve of the propeller under test is reported in red. (b)-(d): Simulated torque waveform at mid-range value of the propeller mechanical characteristics, i.e., $\omega_m = 4500\text{rpm}$ and $T_{\text{avg}} = 0.0972\text{Nm}$, for BLDC control (top) and FOC (bottom).

were employed to approximate as well as possible the real motor control operation. In order to highlight the effect of the driving techniques, position/speed information was provided to the controllers.

In particular, a grid of speed and duty-cycle values was used to impose the simulation settings for the BLDC control: the resulting average torque, rms torque, average total motor power, and average resistive power were collected, so that the desired maps were obtained via interpolation. Similarly, the

power values were collected for FOC, at given constant speed, imposing the current controller (a standard PI with back-EMF compensation) to track constant torque references.

The results are reported in Figures 3-4, where, for completeness, we indicated the experimental speed-torque characteristic of the propeller T-Motor CFProp 13×4.4 L. Note that BLDC control exceeds the theoretical 10% losses increase that would occur under ideal current actuation. In particular, we obtained along the propeller characteristic a motor efficiency difference of 3.65%, 1.49% and 0.54%, evaluated at 3000rpm, 4500rpm, and 6000rpm, respectively. For this reason, FOC is expected to outperform BLDC control efficiency if the same carrier frequency is adopted. In the experimental tests, it was necessary to increase the sampling frequency of the BLDC control for a satisfactory performance of the Zero-Crossing algorithm. However, despite the resulting advantage for the BLDC control, we will show that the efficiency of FOC remains higher throughout the operative range.

On the other hand, the torque distortion in FOC operation is significantly reduced, as highlighted in Figure 4. This result is seen both in the 2D maps of the electric torque ripple, computed as $\sqrt{T_{\text{rms}}^2 - T_{\text{avg}}^2}/T_{\text{avg}}$ (percentage values), and in the example waveforms in the mid-range value of the propeller characteristic (4500rpm). In particular, for the selected operating condition, both controllers were simulated with a large interval (4s) to compute T_{rms} and T_{avg} , leading to a particularly accurate estimation of the ripple values, given by 32.7% (FOC) and 54.4% (BLDC control).

IV. THE PROPOSED CONTROL STRUCTURE

We now introduce a computational-effective sensorless FOC strategy, centered on the framework adopted in [16]. The goal is to develop an output-feedback controller that regulates the

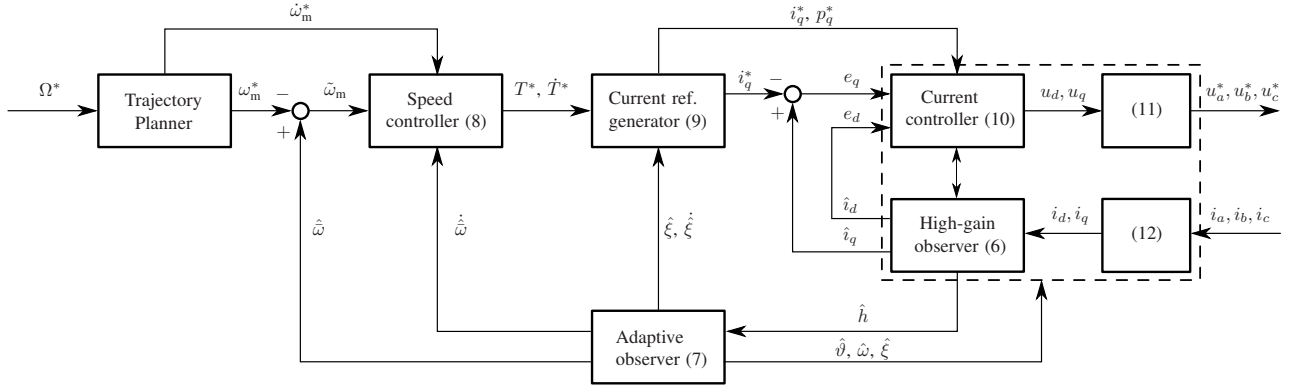


Fig. 5: Structure of the proposed control solution. The scheme is interfaced to the controlled system as shown in Figure 2.

rotor mechanical speed ω_m to a reference ω_m^* , available for design along its derivative $\dot{\omega}_m^*$. The only known system parameters are R , L , and p , while the sole available measurements are given by the stator currents. Here, the fundamental idea is to exploit a re-parametrization of the PMSM dynamics that highlights the position estimation error as a synchronization error between frames. For simplicity, we assume ω positive during all UAV operation, in order to continuously generate thrust for flight maneuvering². Consider, in place of the generic representation frame ϑ_r , the rotor position estimation $\hat{\vartheta}$, with $\hat{\vartheta} = \hat{\omega}$ and $\hat{\omega}$ to be appropriately designed. By letting $\tilde{\vartheta} = \vartheta - \hat{\vartheta}$, $\chi = \omega/\varphi_e$, $\xi = 1/\varphi_e$, $h_d = \chi \sin(\tilde{\vartheta})$, $h_q = -\chi \cos(\tilde{\vartheta})$, the following PMSM dynamics hold:

$$\begin{aligned} \frac{d}{dt}i_d &= -\frac{R}{L}i_d + \frac{h_d + u_d}{L} + \hat{\omega}i_q & \dot{\tilde{\vartheta}} &= \chi\xi - \hat{\omega}. \\ \frac{d}{dt}i_q &= -\frac{R}{L}i_q + \frac{h_q + u_q}{L} - \hat{\omega}i_d \end{aligned} \quad (5)$$

Note that the frames given by ϑ and $\hat{\vartheta}$ achieve synchronization only if $h_d \rightarrow 0$. The back-EMF vector $h = (h_d, h_q)^T$ is unavailable for control, yet we can replace its measurement with a suitable estimate by means of a high-gain observer:

$$\begin{aligned} \dot{\hat{i}}_d &= -\frac{R}{L}\hat{i}_d + \frac{\hat{h}_d + u_d}{L} + \hat{\omega}i_q + k_p\tilde{i}_d, & \dot{\hat{h}}_d &= k_i\tilde{i}_d \\ \dot{\hat{i}}_q &= -\frac{R}{L}\hat{i}_q + \frac{\hat{h}_q + u_q}{L} - \hat{\omega}i_d + k_p\tilde{i}_q, & \dot{\hat{h}}_q &= k_i\tilde{i}_q \end{aligned} \quad (6)$$

with k_p and k_i positive scalars and $\tilde{i}_d = i_d - \hat{i}_d$, $\tilde{i}_q = i_q - \hat{i}_q$ the current estimation errors. The back-EMF estimate $\hat{h} = (\hat{h}_d, \hat{h}_q)^T$ can be used to design an adaptive attitude observer, which is chosen as follows:

$$\dot{\hat{\vartheta}} = \hat{\xi}\sqrt{\hat{h}_d^2 + \hat{h}_q^2} + k_\eta\hat{h}_d = \hat{\omega}, \quad \dot{\hat{\xi}} = \gamma\hat{h}_d, \quad (7)$$

where k_η and γ are positive gains. In addition, let $\hat{\omega} = \hat{\xi}\sqrt{\hat{h}_d^2 + \hat{h}_q^2}/p$ be the estimated mechanical speed, and note that the term $k_\eta\hat{h}_d$ in $\hat{\omega}$ is omitted to reduce sensitivity to measurement noise. The observer (6)-(7) was proven in [16] to have a regional practical asymptotic stability characterization³, as long as the speed ω is far from zero and with bounded derivative during all operation.

²See [16] for a more general representation accounting for both speed signs.

³Notably, the domain of attraction is very close to the entire state space.

The controller structure can be then completed with a nested stabilizer for reference torque generation and current tracking. Denote with $\tilde{\omega}_m = \hat{\omega} - \omega_m^*$ the estimated speed mismatch, and consider the following PI controller:

$$\begin{aligned} T^* &= -k_{p\omega}\tilde{\omega}_m + \sigma_\omega, & \dot{\sigma}_\omega &= -k_{i\omega}\tilde{\omega}_m \\ \dot{T}^* &= -k_{p\omega}\dot{\tilde{\omega}} + k_{p\omega}\dot{\omega}_m^* - k_{i\omega}\tilde{\omega}_m, \end{aligned} \quad (8)$$

with $k_{p\omega}$ and $k_{i\omega}$ positive scalars. Note that, for simplicity, we do not introduce feedforward terms in T^* to account for the load or the derivative $\dot{\omega}_m^*$. Exploiting the estimation of $\xi = 1/\varphi_e$ provided by the attitude observer, we can directly translate the torque reference and its derivative into corresponding signals associated with the current i_q :

$$i_q^* = \frac{2}{3p}\hat{\xi}T^*, \quad p_q^* = \frac{2}{3p}\left(\dot{\hat{\xi}}T^* + \hat{\xi}\dot{T}^*\right). \quad (9)$$

The remaining step in the control design consists of tracking a current signal of the form $(0, i_q^*)$. Consider the estimated current mismatch errors $e_d = \hat{i}_d$, $e_q = \hat{i}_q - i_q^*$. As shown in the following, defining the errors with the estimated currents instead of the measured ones is motivated by the simple stability analysis. We can assign the input voltages as follows:

$$\begin{aligned} u_d &= -\hat{h}_d - L(\hat{\omega}i_q + k_{pe}e_d) + \sigma_d, & \dot{\sigma}_d &= -k_{ie}e_d \\ u_q &= Ri_q^* - \hat{h}_q + L(\hat{\omega}i_d + p_q^* - k_{pe}e_q) + \sigma_q, & \dot{\sigma}_q &= -k_{ie}e_q, \end{aligned} \quad (10)$$

with k_{pe} , k_{ie} positive gains for tuning.

Finally, we recall the transformations involved in the conversion of signals from the rotating two-phase to the three-phase representation and vice-versa:

$$\begin{aligned} \begin{pmatrix} u_\alpha \\ u_\beta \end{pmatrix} &= \begin{pmatrix} \cos(\hat{\vartheta}) & -\sin(\hat{\vartheta}) \\ \sin(\hat{\vartheta}) & \cos(\hat{\vartheta}) \end{pmatrix} \begin{pmatrix} u_d \\ u_q \end{pmatrix} \\ \begin{pmatrix} u_a^* \\ u_b^* \\ u_c^* \end{pmatrix} &= \begin{pmatrix} 1 & 0 \\ -0.5 & \sqrt{3}/2 \\ -0.5 & -\sqrt{3}/2 \end{pmatrix} \begin{pmatrix} u_\alpha \\ u_\beta \end{pmatrix}, \end{aligned} \quad (11)$$

$$\begin{pmatrix} i_\alpha \\ i_\beta \end{pmatrix} = \frac{2}{3} \begin{pmatrix} 1 & -0.5 & -0.5 \\ 0 & \sqrt{3}/2 & -\sqrt{3}/2 \end{pmatrix} \begin{pmatrix} i_a \\ i_b \\ i_c \end{pmatrix} \quad (12)$$

$$\begin{pmatrix} i_d \\ i_q \end{pmatrix} = \begin{pmatrix} \cos(\hat{\vartheta}) & \sin(\hat{\vartheta}) \\ -\sin(\hat{\vartheta}) & \cos(\hat{\vartheta}) \end{pmatrix} \begin{pmatrix} i_\alpha \\ i_\beta \end{pmatrix}.$$

The overall scheme is shown in Figure 5, and a generic trajectory planner is also reported to convert a speed command Ω^* (requested, e.g., by a flight controller), into suitable references ω_m^* , $\dot{\omega}_m^*$. The detailed description of this block is out of the scope of the analysis.

A. Error System Analysis and Tuning

In addition to the above structure, we provide some considerations to appropriately tune the controller, based on the simplifying assumption that $\dot{\omega}_m^* = 0$. These arguments rely on the linearization of the error system and allow to draw a simple local stability analysis. In this context, formal robustness guarantees can be provided also for the case $\dot{\omega}_m^* \neq 0$. We begin by defining the error equations.

Let $\tilde{v} = (\tilde{v}_d, \tilde{v}_q)^T$, $\tilde{h} = (\tilde{h}_d, \tilde{h}_q)^T = (h_d - \hat{h}_d, h_q - \hat{h}_q)^T = h - \hat{h}$, and $\tilde{\xi} = \xi - \hat{\xi}$. Recall the observer error dynamics in [16], with the high-gain estimation error:

$$\dot{\tilde{v}} = -(R/L + k_p)\tilde{v} + \tilde{h}/L, \quad \dot{\tilde{h}} = -k_i\tilde{v} + \dot{h}, \quad (13)$$

and the attitude observer reconstruction error:

$$\dot{\tilde{\vartheta}} = \chi(\tilde{\xi} - k_\eta \sin(\tilde{\vartheta})) + \delta_1, \quad \dot{\tilde{\xi}} = -\gamma\chi \sin(\tilde{\vartheta}) + \delta_2, \quad (14)$$

where both δ_1 and δ_2 vanish in $\tilde{h} = 0$. Here, we include the dynamics of the estimated current mismatch dynamics and of the speed tracking error, highlighting the shape of \dot{h} in (13), which represents a disturbance for the back-EMF reconstruction. Let $e = (e_d, e_q)^T$, $\sigma = (\sigma_d, \sigma_q)^T$, then it holds:

$$\dot{e} = -(R/L + k_{pe})e + \sigma/L + k_p\tilde{v}, \quad \dot{\sigma} = -k_{ie}e \quad (15)$$

To compute the speed dynamics, we first factorize by Taylor expansion the speed estimation error, for $\omega > 0$ and \tilde{h} sufficiently small:

$$p(\hat{\omega} - \omega_m) = \hat{\xi}|\hat{h}| - \xi|h| = (\xi - \tilde{\xi})|h - \tilde{h}| - \xi|h| \\ = -p(\tilde{\xi}/\xi)\omega_m + (\tilde{\xi} - \xi)\delta_3(h, \tilde{h}) \quad (16)$$

where δ_3 vanishes in $\tilde{h} = 0$. Denote with $e_\omega = \omega_m - \omega_m^*$ the tracking error, then it holds ($\tilde{\omega}_m = e_\omega + \hat{\omega} - \omega_m$, $\dot{\omega}_m^* = 0$):

$$J\dot{e}_\omega = (3p\varphi_e/2)\cos(\tilde{\vartheta})i_q^* - c_1(\omega_m^* + e_\omega) - c_2(\omega_m^* + e_\omega)^2 + \\ + (3p\varphi_e/2)(\tilde{v}_q + e_q)\cos(\tilde{\vartheta}) - (3p\varphi_e/2)(\tilde{v}_d + e_d)\sin(\tilde{\vartheta}) \\ = \frac{\xi - \tilde{\xi}}{\xi}\cos(\tilde{\vartheta})\left[\sigma_\omega - k_{p\omega}e_\omega + k_{p\omega}\frac{\tilde{\xi}}{\xi}(\omega_m^* + e_\omega)\right] + \\ - d_0 - d_1e_\omega - c_2e_\omega^2 + \delta_4(\xi, \tilde{\xi}, \tilde{\vartheta}, h, \tilde{h}) + \\ + (3p\varphi_e/2)(\tilde{v}_q + e_q)\cos(\tilde{\vartheta}) - (3p\varphi_e/2)(\tilde{v}_d + e_d)\sin(\tilde{\vartheta}) \quad (17)$$

where d_0, d_1 are positive scalars and δ_4 a map vanishing in $\tilde{h} = 0$. Consider $\tilde{\sigma}_\omega = \sigma_\omega - d_0$, with associated dynamics:

$$\dot{\tilde{\sigma}}_\omega = -k_{i\omega}e_\omega + k_{i\omega}(\tilde{\xi}/\xi)(\omega_m^* + e_\omega) + \delta_5(\xi, \tilde{\xi}, h, \tilde{h}), \quad (18)$$

with δ_5 vanishing in $\tilde{h} = 0$. Since $\chi = |h| = (p/\xi)(\omega_m^* + e_\omega)$, we have

$$\dot{h} = \frac{p}{\xi}\dot{e}_\omega \begin{pmatrix} \sin(\tilde{\vartheta}) \\ -\cos(\tilde{\vartheta}) \end{pmatrix} + \frac{p}{\xi}(\omega_m^* + e_\omega) \begin{pmatrix} \cos(\tilde{\vartheta}) \\ \sin(\tilde{\vartheta}) \end{pmatrix} (\omega - \hat{\omega}), \quad (19)$$

where in particular the second term vanishes in $\tilde{h} = 0$, $\tilde{\vartheta} = 0$, $\tilde{\xi} = 0$. This means that the error system (13)-(14)-(15)-(17)-(18) has an equilibrium in the origin, whose local stability analysis can be performed via two time-scales arguments. In particular, we impose the dynamics (13)-(15) to be the fast subsystem, while we leave the attitude estimation error (14) and the speed dynamics (17)-(18) as the slow subsystem.

Consider system (13). Following the same arguments as in [16], we select k_p, k_i by placing the roots of the polynomial

$$P_1(\lambda) = \lambda^2 + (R/L + k_p)\lambda + k_i/L \quad (20)$$

in $\varepsilon^{-1}\{\lambda_1, \lambda_2\}$, where the pair $\{\lambda_1, \lambda_2\}$ is a design choice and ε is a positive scalar. System (15) is cascade-interconnected with the previous one, hence we similarly choose k_{pe}, k_{ie} to place the roots of the polynomial

$$P_2(\lambda) = \lambda^2 + (R/L + k_{pe})\lambda + k_{ie}/L \quad (21)$$

in $\varepsilon^{-1}\{\lambda_{1e}, \lambda_{2e}\}$. The parameter ε is then employed as perturbation parameter, and time-scale separation can be imposed by choosing it sufficiently small, i.e. by imposing sufficiently high gains. In particular, analysis can be performed considering two simplified limit systems as $\varepsilon \rightarrow 0^+$ [24, Chapter 11]: the boundary-layer system and the reduced-order model.

The reduced-order model, corresponding to the slow subsystem as $\tilde{v} = \tilde{h} = e = \sigma = 0$, is analyzed by linearization of the dynamics. The attitude estimation error, given by the dynamics of $(\tilde{\vartheta}, \tilde{\xi})$, corresponds to the following system:

$$\dot{y} = \frac{p\omega_m^*}{\xi} \begin{pmatrix} -k_\eta & 1 \\ -\gamma & 0 \end{pmatrix} y, \quad (22)$$

whose eigenvalues can be assigned with k_η, γ , exploiting a priori flux information and the range of speed references for flight control. On the other hand, the linearization of the speed tracking error dynamics, associated with $(e_\omega, \tilde{\sigma}_\omega)$, is given by:

$$\dot{z} = \begin{pmatrix} -\frac{k_{p\omega} + d_1}{J} & \frac{1}{J} \\ -k_{i\omega} & 0 \end{pmatrix} z + \frac{1}{\xi} \begin{pmatrix} k_{p\omega}\omega_m^* - d_0 \\ k_{i\omega}\omega_m^* \end{pmatrix} (0 \ 1) y, \quad (23)$$

which is cascade-interconnected with (22), hence $k_{p\omega}, k_{i\omega}$ can be chosen independently from k_η, γ . Finally, we can summarize the local stability properties of the proposed controller.

Proposition 1. Consider a constant reference ω_m^* , satisfying $0 < \underline{\Omega} \leq \omega_m^* \leq \overline{\Omega}$, with positive scalars $\underline{\Omega}, \overline{\Omega}$. Pick, and fix, arbitrary positive scalars $k_\eta, \gamma, k_{p\omega}, k_{i\omega}$, and choose $\lambda_1, \lambda_2, \lambda_{1e}, \lambda_{2e}$ such that the polynomials $P_1(\cdot)$ and $P_2(\cdot)$ are Hurwitz, for any $\varepsilon > 0$. Then, there exists $\varepsilon^* > 0$ such that, for all ε satisfying $0 < \varepsilon < \varepsilon^*$, the origin of the error system (13)-(14)-(15)-(17)-(18) is locally exponentially stable.

Proof. The analysis is similar to [16, Proposition 1]. In particular, the boundary layer system is globally exponentially stable by design of $\lambda_1, \lambda_2, \lambda_{1e}, \lambda_{2e}$, while the reduced-order model is locally exponentially stable. Furthermore, the vector field and its partial derivatives, up to second order, are bounded in a neighborhood of the origin, since $\omega_m^* \neq 0$ and thus $|\hat{h}|$ is twice differentiable in its arguments. It is then sufficient to notice that the origin of the error system is an isolated

TABLE II: Possible Implementation Sequence and Computational Burden of the Proposed Solution

	Sums	Multiplications	Comparisons	Sq. Root & SinCos	Number of States
Adaptive observer (7) with wrap (25)	2 or 3	6	2	1	2
Computation of $\dot{\hat{\omega}}$ (eq. (28))	1	1	0	0	1
Speed controller (8)	4	4	0	0	1
Current ref. generator (9)	1	5	0	0	0
Coordinate transformation (12)	5	7	0	2	0
Current controller (10)	9	9	0	0	2
High-gain observer (6) or (24)	10 (7)	10 (8)	0	0	4
Coordinate transformation (11)	4	4	0	2 (0)	0

equilibrium, for any bounded $\varepsilon > 0$, to guarantee that all sufficient conditions of [24, Theorem 11.4] hold. \square

The practical relevance of this result is due to the inherent robustness to small perturbations (such as small values of $\dot{\omega}_m^*$) ensured by the theorem of total stability [25, Theorem 10.2.1]. Notably, we can re-define the error of the speed integrator as $\tilde{\sigma}_\omega = \sigma_\omega - d_0 - J\dot{\omega}_m^*$, thus indicating that weaker singular perturbations results [24, Theorems 11.1-11.2] can be applied in time intervals such that $\underline{\Omega} \leq \omega_m^* \leq \overline{\Omega}$ and $\dot{\omega}_m^*$ is continuous. This means that the proposed controller is also effective in time-varying scenarios, as long as $\varepsilon > 0$ is sufficiently small.

B. Computational Analysis and Implementation Details

We conclude the description of the proposed controller with an analysis of the computational effort. The complexity of the structure revolves around the evaluation of the mathematical operations on the right-hand side of equations from (6) to (12), including the computation of some auxiliary signals. In this analysis, we do not consider the controller discretization, since the corresponding burden is heavily affected by the chosen algorithm. For clarity, in Section V we will also indicate the cost associated with our discretization choices. The overall data are reported in Table II, with the controller components indicated in a possible implementation sequence (from top to bottom). We remark that the adaptive observer was separated from the computation of $\dot{\hat{\omega}}$, as motivated in the following.

Some comments are needed to explain the indicated values. Firstly, the values outside the parentheses are the minimum operations needed if each controller component is treated as an independent block, with input/output signals corresponding to those in Figure 5 (and the error signals computed in the first block they are needed). Within the parentheses, instead, we indicated the computations achieved with some optimization between the blocks. On the one hand, the trigonometric functions are counted once and indicated in the first component that includes them. On the other hand, an alternative to the high-gain observer (6) is obtained by replacing u_d and u_q with the expressions in (10), leading to:

$$\begin{aligned} \dot{\hat{i}}_d &= -\left(k_{pe} + \frac{R}{L}\right)e_d + \frac{\sigma_d}{L} + k_p \tilde{i}_d, & \dot{\hat{h}}_d &= k_i \tilde{i}_d \\ \dot{\hat{i}}_q &= -\left(k_{pe} + \frac{R}{L}\right)e_q + \frac{\sigma_q}{L} + k_p \tilde{i}_q + p_q^*, & \dot{\hat{h}}_q &= k_i \tilde{i}_q, \end{aligned} \quad (24)$$

which allows a slight reduction of the number of operations. We also remark that the computation of e_q in the observer (24) is redundant, since it is already available from (10).

Concerning the adaptive attitude observer, the implementation is based on wrapping the estimated angle at each time:

$$\text{wrap}(\hat{\vartheta}) = \begin{cases} \hat{\vartheta} + 2\pi & \text{if } \hat{\vartheta} < -\pi \\ \hat{\vartheta} & \text{if } \hat{\vartheta} \in [-\pi, \pi] \\ \hat{\vartheta} - 2\pi & \text{if } \hat{\vartheta} > \pi, \end{cases} \quad (25)$$

which requires two comparisons at each evaluation and an additional sum in case of underflow or overflow. In this respect, the values in Table II correspond to the common situation where $\hat{\vartheta}(0) \in [-\pi, \pi]$ and the distance between consecutive samples of $\hat{\vartheta}$ is below 2π .

It is also meaningful to investigate the implementation of $\dot{\hat{\omega}}$. In particular, the computation in exact form is the following:

$$\dot{\hat{\omega}} = \frac{\hat{\xi}}{p} \sqrt{\hat{h}_d^2 + \hat{h}_q^2} + k_i \frac{\hat{\xi}}{p} \frac{\hat{h}_d \tilde{i}_d + \hat{h}_q \tilde{i}_q}{\sqrt{\hat{h}_d^2 + \hat{h}_q^2}}, \quad (26)$$

which has a singularity in $\hat{h}_d = \hat{h}_q = 0$. Denoting $(\hat{h}_d, \hat{h}_q) = r(\cos(\psi), \sin(\psi))$, for $r \geq 0$ and $\psi \in (-\pi, \pi]$, it holds:

$$\dot{\hat{\omega}} = \frac{\hat{\xi}}{p} r + k_i r \frac{\hat{\xi}}{p} \frac{\cos(\psi) \tilde{i}_d + \sin(\psi) \tilde{i}_q}{r}, \quad (27)$$

therefore, for any ψ , the limit as $r \rightarrow 0^+$ exists and is finite. Since this limit is not unique, a possible implementation procedure if r is close to 0 consists of preserving the previous value of ψ and simplifying r . In this work, for computational simplicity, we opt instead to approximate $\dot{\hat{\omega}}$ through a filter:

$$\dot{\hat{\omega}}_f = -k_f(\hat{\omega}_f - \dot{\hat{\omega}}), \quad y_f = -k_f(\hat{\omega}_f - \dot{\hat{\omega}}), \quad (28)$$

where k_f is a positive scalar, while y_f is used to replace $\dot{\hat{\omega}}$ in the expression of \dot{T}^* . The computations of the filter are reported in a separate row in Table II. By choosing k_f sufficiently large, it is possible to ensure an accurate estimate of $\dot{\hat{\omega}}$. This fact is motivated by singular perturbations arguments, since the resulting dynamics can be included in the error system analysis, without modifying the result in Proposition 1. Finally, we remark that the initialization $\hat{\omega}_f(0) = \dot{\hat{\omega}}(0)$ is a convenient choice to mitigate the initial transient behavior.

V. EXPERIMENTAL RESULTS

A. Experimental Setup

The main components of the equipment are the following: an Aim-TTi CPX400DP bench power supply, a LeCroy HDO4054 four-channel oscilloscope and an aluminum frame to suspend a T-Motor Antigravity-4006-KV380, coupled with a T-Motor CFProp 13×4.4 L Propeller. In addition, we

equipped the motor with a 14bit-resolution on-axis magnetic rotary encoder (AD5047D-EK-AB encoder evaluation kit and AS5000-MD6H-2 diametric magnet), in order to compare the sensorless control algorithms with a common speed-position information source (clearly, the encoder was employed for analysis and not for feedback). Two separate electronic devices were deployed: a commercial electronic speed controller T-Motor ALPHA 40A LV and a custom power converter, endowed with a Mosfet-VSI, and a Cortex-M4 digital controller operated with a lightweight Hard Real-Time Operating System (developed by our team) that was synchronized with the inverter PWM carrier. This board was used to host, apart from the control algorithms of the following subsections, also a position/speed acquisition routine to elaborate the encoder data for analysis. The experimental setup is depicted in Figure 6, where the main components can be clearly identified.

B. Efficiency and Accuracy Comparison

The algorithms that we use for comparison are the proposed controller, the commercial FOC T-Motor ALPHA 40A LV, tuned specifically by the manufacturer for the motor and propeller under test, and a custom sensorless BLDC controller with Zero-Crossing detection. Since the power electronics of the three algorithms is not the same, only the absorbed motor power is considered, whereas power converter contributions are excluded: this is consistent with the simulation results of Section III. To make the comparisons as reliable as possible, the proposed FOC was implemented at a sampling frequency of 15kHz, corresponding to that of T-Motor ALPHA 40A LV.

Discrete-time versions of the controller and observer units were developed with the forward Euler method, except for the estimated current dynamics in (6), where we employed the matrix exponential. From a computational point of view, the forward Euler discretization involved a sum and a multiplication for each state (for a total of 8 states), while the matrix exponential led to an increase of the operations by

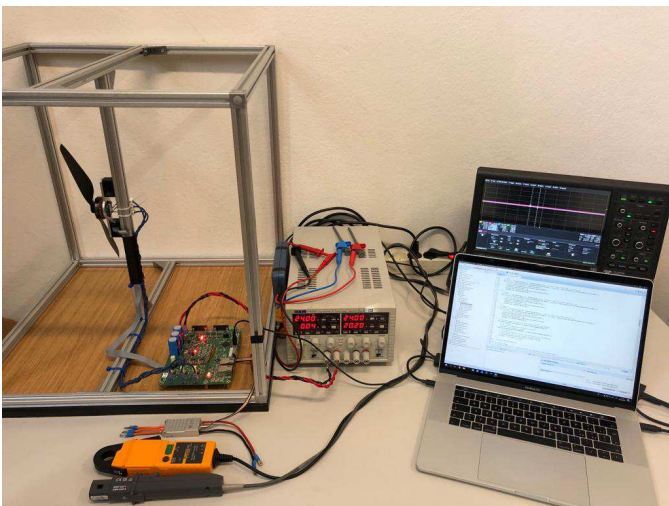


Fig. 6: Experimental setup for the efficiency/accuracy tests. The voltage and current probes are shown unconnected in order to display more clearly the custom power converter, in the picture connected to the motor and the power supply.

TABLE III: Tuning Parameters of the Proposed Controller

k_p	1178	k_i	340	$\frac{\lambda_{1,2}}{\varepsilon}$	$(-2.36 \pm 2.36i) \times 10^3$
k_{pe}	964	k_{ie}	154.6	$\frac{\lambda_{1e,2e}}{\varepsilon}$	-2357, -2142
k_η	115.8	γ	6707	$\lambda_{1s,2s}$	$(-4.29 \pm 4.29i) \times 10^2$
$k_{p\omega}$	7.1×10^{-3}	$k_{i\omega}$	41.7×10^{-3}	$\lambda_{1\omega,2\omega}$	-46.6, -6.3

one multiplication for each state (for the remaining 2 states). In addition, we adopted a fixed-point implementation (with scaling chosen for each signal), to comply with the deadline imposed by the sampling frequency. Besides, a look-up table and the CORDIC algorithm were employed to evaluate the square root and the trigonometric functions, respectively. The algorithm was finally obtained through code generation from a Simulink model. A precise evaluation of the computational time, from sensor acquisition to the PWM level assignment, was retrieved experimentally while running the algorithm on a Cortex-M4 with 144MHz clock frequency. This way, we established with 1000 evaluations an average elapsed time of $24.2\mu s$, with minimum and maximum values given by $21.2\mu s$ and $26.3\mu s$, respectively. These results were obtained without the need of a floating-point unit, and including several overheads due to measurement processing and voltage actuation.

The adopted controller gains are reported in Table III, with the perturbation parameter chosen as $\varepsilon = 1.5L/R = 4.24 \times 10^{-4}$, along with the corresponding subsystem eigenvalues (see the last column in Table III). These values stem from the solutions of (20), (21) for the current observer and controller, and from the state matrices of the linearized systems (22), (23). For the latter, we considered the linearization around a point corresponding to the mean value of the speed range, i.e., 4500rpm, load inertia $J = 1.43 \times 10^{-4} \text{Kg m}^2$ and load coefficients $c_1 = 1.25 \times 10^{-4} \text{Nms/rad}$, $c_2 = 0.3 \times 10^{-6} \text{Nms}^2/\text{rad}^2$ (estimated values from the Simulink model for code generation), leading to the coefficient $d_1 = 4.08 \times 10^{-4} \text{Nms/rad}$. Finally, it was sufficient to choose $k_f = 500$ to ensure a satisfactory approximation of $\hat{\omega}$. On the other hand, the BLDC controller was implemented at 40kHz, since the sampling of all data in the development board is aligned with the PWM frequency, therefore keeping 15kHz was insufficient to obtain a precise Zero-Crossing at high mechanical speed. Indeed, at 6000rpm, the sextant frequency is 7.2kHz; thus, at 15kHz, only approximately two samples are acquired for each sextant.

Two experimental comparisons are presented. All controllers were tested for their efficiency performance under constant speed conditions, while only the FOC algorithms were analyzed from the accuracy viewpoint, considering some aggressive time-varying speed references.

The power absorption experiments were performed driving the motor at constant mechanical speed, computing for each operating point the total power of the motor reading two phase currents and two line voltages (Aron connection), and obtaining the resistive power from the sampled currents (computing the third from the star connection) considering the motor resistance $R = 108 \text{m}\Omega$, measured at a temperature close to the operating one. The results are shown in Figure 7, where an efficiency estimation from total and resistive

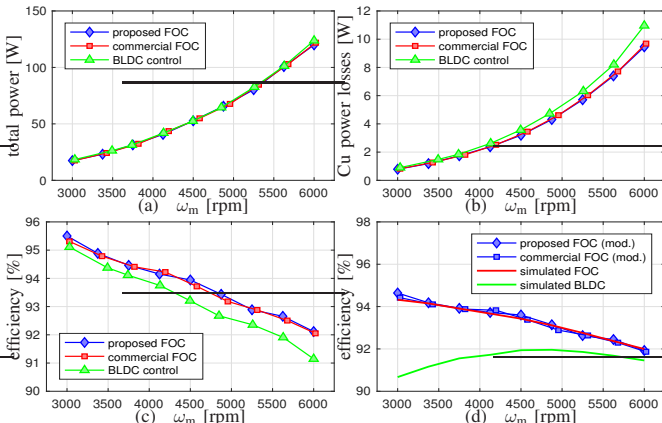


Fig. 7: Efficiency comparative analysis. (a): total power measured with an Aron connection to the motor. (b): resistive losses, computed with the current measurements and assuming R as in Table I. (c): efficiency computed assuming the resistive power as only power loss source. The proposed controller is in blue, T-Motor ALPHA 40A LV is in red, while the BLDC controller is indicated in green. (d): comparison between the simulated FOC efficiency (red) and the corresponding experimental results, considering as total power the experimental data reduced by 2.8W. The simulated BLDC control efficiency at 15kHz is also shown (in green).

power is also indicated⁴. As expected from the preliminary estimations and the simulation analysis, the FOC algorithms outperform the BLDC controller, despite the non-perfectly sinusoidal back-EMF of the motor (see Figure 1-(a)-(e)-(i)) and the significantly lower current ripple due to the higher PWM frequency of the adopted BLDC control. Indeed, the improvement of the motor's efficiency achieved by FOC, compared to BLDC control, is 0.4%, 0.77%, and 0.98% at 3000rpm, 4500rpm, and 6000rpm, respectively. Note that the resistive losses of the commercial FOC and the proposed controller are matched with the simulation results, indicating that both these algorithms provide a very accurate position reconstruction in steady-state conditions. However, the FOC total powers have a relatively constant difference between simulations and experiments: in Figure 7-(d) we show the resulting efficiency, obtained reducing the experimental total powers by a constant offset of 2.8W. Since this graph displays, with satisfactory precision (up to probe numeric errors), a proper matching between simulation and experimental data, we suggest that the mismatch is possibly introduced by iron losses and the non-ideal sinusoidal shape of T-Motor-Antigravity-4006-KV380. In Figure 7-(d) we also indicated the simulated BLDC control efficiency at 15kHz, highlighting the improvement expected from FOC if all controllers were implemented at the same frequency.

Finally, we show how the proposed FOC controller performs with variable speed references. In Figure 8, we indicated the comparison between the proposed controller and T-Motor ALPHA 40A LV, considering different scenarios that highlight the dynamic behavior of the two controllers: in particular,

⁴Due to motor heating and unaccounted iron losses, the computed efficiency overestimates the actual one, but the mismatch is not expected to be large.

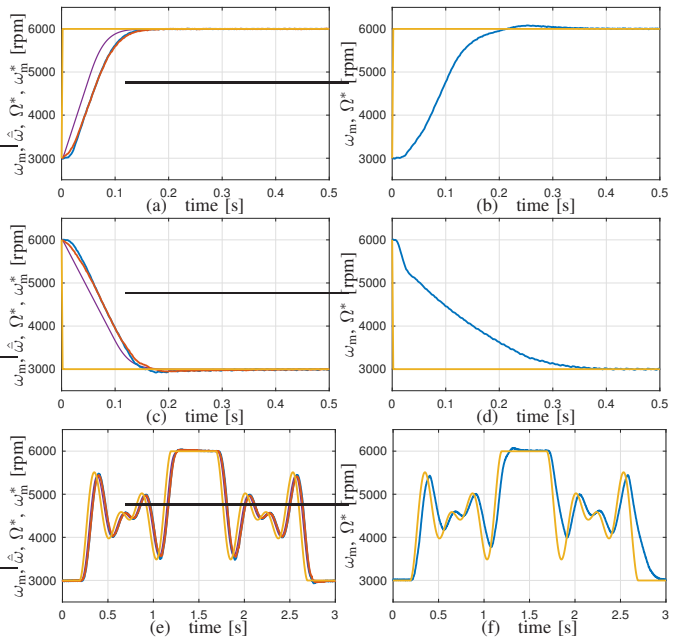


Fig. 8: Accuracy comparison between the proposed controller and T-Motor ALPHA 40A LV. The responses of the proposed solution are in (a)-(c)-(e), with encoder speed (blue), estimated speed (red), and references Ω^* (yellow) and ω_m^* (violet), while the responses of T-Motor ALPHA 40A LV are in (b)-(d)-(f), with encoder speed (blue) and reference speed Ω^* (yellow).

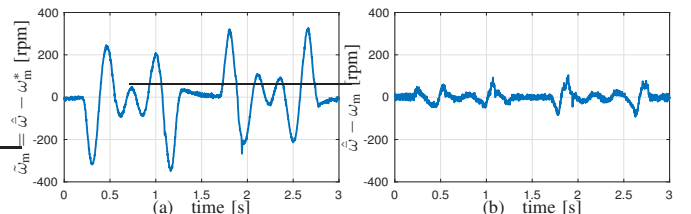


Fig. 9: Tracking performance of the proposed controller for the sinusoidal reference scenario of Figure 8-(e). (a): estimated speed mismatch. (b): speed estimation error.

positive and negative step references and amplitude-modulated sinusoids were considered. In these tests, we indicated the observer's estimated speed, $\hat{\omega}$, to validate the variable-speed tracking features proven in [16]. Notably, the proposed controller displays a generally exponential transient response, in addition to a higher consistency when tracking challenging time-varying references. The accuracy of our scheme in the sinusoidal reference scenario is further highlighted in Figure 9, where we indicated the estimated speed mismatch and the speed estimation error. Consequently, in light of the achieved tracking performance, the proposed solution is expected to be particularly suitable for aggressive UAV maneuvering.

VI. CONCLUSIONS

We presented a comparative study, based on simulation and experimental results, between different control strategies employed for the electric propulsion of UAVs. Starting from the physical characteristics of the motors adopted in this field, we showed the benefits of FOC over BLDC control, resulting in higher efficiency and longer flight duration. A

low-complexity sensorless controller was presented to achieve high performance in aggressive speed reference tracking. The proposed controller still depends, for correct implementation, on accurate knowledge of stator resistance and inductance: future efforts will be dedicated to supplying this information online with adaptive and system identification techniques. Addressing this aspect will be critical, in the next years, to comply with the ever-growing performance and robustness requirements for Unmanned Aerial Vehicles.

REFERENCES

- [1] "Study analysing the current activities in the field of UAV," European Commission, Tech. Rep., 2014.
- [2] T. H. Cox, C. J. Nagy, M. A. Skoog, and I. A. Somers, "Civil UAV capability assessment," NASA, Tech. Rep., December 2004.
- [3] K. P. Valavanis, *Advances in unmanned aerial vehicles: state of the art and the road to autonomy*. Springer Science & Business Media, 2008, vol. 33.
- [4] D. Yang, Q. Wu, Y. Zeng, and R. Zhang, "Energy tradeoff in ground-to-UAV communication via trajectory design," *IEEE Transactions on Vehicular Technology*, vol. 67, no. 7, pp. 6721–6726, 2018.
- [5] F. Morbidi, R. Cano, and D. Lara, "Minimum-Energy path generation for a quadrotor UAV," in *2016 IEEE International Conference on Robotics and Automation (ICRA)*. IEEE, May 2016, pp. 1492–1498.
- [6] R. D'Sa, D. Jenson, T. Henderson, J. Kilian, B. Schulz, M. Calvert, T. Heller, and N. Papanikolopoulos, "SUAV: Q-An improved design for a transformable solar-powered UAV," in *2016 IEEE/RSJ International Conference on Intelligent Robots and Systems (IROS)*. IEEE, 2016, pp. 1609–1615.
- [7] S. Driessens and P. Pounds, "The triangular quadrotor: a more efficient quadrotor configuration," *IEEE Transactions on Robotics*, vol. 31, no. 6, pp. 1517–1526, 2015.
- [8] R. A. Sowah, M. A. Acquah, A. R. Ofofi, G. A. Mills, and K. M. Koumadi, "Rotational energy harvesting to prolong flight duration of quadcopters," *IEEE Transactions on Industry Applications*, vol. 53, no. 5, pp. 4965–4972, 2017.
- [9] P. Pounds, R. Mahony, and P. Corke, "System identification and control of an aerobot drive system," in *2007 Information, Decision and Control*. IEEE, 2007, pp. 154–159.
- [10] T.-H. Kim, H.-W. Lee, and M. Ehsani, "State of the art and future trends in position sensorless brushless DC motor/generator drives," in *31st Annual Conference of IEEE Industrial Electronics Society, 2005. IECON 2005*. IEEE, 2005, pp. 8–pp.
- [11] P. P. Acarnley and J. F. Watson, "Review of position-sensorless operation of brushless permanent-magnet machines," *IEEE Transactions on Industrial Electronics*, vol. 53, no. 2, pp. 352–362, 2006.
- [12] Ø. Magnussen, G. Hovland, M. Ottestad, and S. Kirby, "Experimental study on the influence of controller firmware on multirotor actuator dynamics," in *2014 IEEE International Symposium on Robotic and Sensors Environments (ROSE) Proceedings*. IEEE, 2014, pp. 106–111.
- [13] O. Solomon and P. Famouri, "Dynamic performance of a permanent magnet brushless dc motor for uav electric propulsion system-part i," in *IECON 2006-32nd Annual Conference on IEEE Industrial Electronics*. IEEE, 2006, pp. 1400–1405.
- [14] A. Bosso, C. Conficoni, and A. Tilli, "Multirotor UAV flight endurance and control: the drive perspective," in *IECON 2016 - 42nd Annual Conference of the IEEE Industrial Electronics Society*. IEEE, 2016, pp. 1839–1845.
- [15] M. Miyamasu and K. Akatsu, "Efficiency comparison between Brushless dc motor and Brushless AC motor considering driving method and machine design," *IEEE Journal of Industry Applications*, vol. 2, no. 1, pp. 79–86, 2013.
- [16] A. Tilli, A. Bosso, and C. Conficoni, "Towards sensorless observers for sinusoidal electric machines with variable speed and no mechanical model: A promising approach for PMSMs," *Systems & Control Letters*, vol. 123, pp. 16–23, January 2019.
- [17] T.-Y. Lee, M.-K. Seo, Y.-J. Kim, and S.-Y. Jung, "Motor design and characteristics comparison of outer-rotor-type BLDC motor and BLAC motor based on numerical analysis," *IEEE Transactions on Applied Superconductivity*, vol. 26, no. 4, pp. 1–6, June 2016.
- [18] W. Leonhard, *Control of electrical drives*. Springer Science & Business Media, 2001.
- [19] Y.-S. Lai, F.-S. Shyu, and Y.-H. Chang, "Novel loss reduction pulsewidth modulation technique for brushless dc motor drives fed by MOSFET inverter," *IEEE Transactions on Power Electronics*, vol. 19, no. 6, pp. 1646–1652, 2004.
- [20] A. Sathyan, N. Milivojevic, Y.-J. Lee, M. Krishnamurthy, and A. Emadi, "An FPGA-based novel digital PWM control scheme for BLDC motor drives," *IEEE Transactions on Industrial Electronics*, vol. 56, no. 8, pp. 3040–3049, 2009.
- [21] C. M. Verrelli and P. Tomei, "Global stability for the inner and outer PI control actions in non-salient-pole PMSMs," *Automatica*, vol. 117, p. 108988, 2020.
- [22] P. Bernard and L. Praly, "Convergence of gradient observer for rotor position and magnet flux estimation of permanent magnet synchronous motors," *Automatica*, vol. 94, pp. 88–93, 2018.
- [23] D. Bazylev, A. Pyrkin, and A. Bobtsov, "Position and speed observer for PMSM with unknown stator resistance," in *2018 European Control Conference (ECC)*. IEEE, 2018, pp. 1613–1618.
- [24] H. K. Khalil, *Nonlinear Systems, Third Edition*. Prentice-Hall, 2002.
- [25] A. Isidori, *Nonlinear Control Systems II*. Springer-Verlag, 1999.



Alessandro Bosso received the Master's Degree in Automation Engineering and the Ph.D. degree in automatic control from the University of Bologna, Italy, in 2016 and 2020, respectively. Currently, he is a postdoctoral researcher at the Department of Electrical, Electronic and Information Engineering (DEI), at the University of Bologna. His research interests include nonlinear control with input and state constraints, nonlinear and distributed adaptive control, hybrid systems, and sensorless control of electric machines.



Christian Conficoni received the Master's Degree in Electronic Engineering, from the University of Bologna, Italy, in 2008. In 2013, he received the Ph.D. degree in automatic control from the same institution. Currently he is a postdoctoral researcher at the Department of Electrical, Electronic and Information Engineering (DEI), at the University of Bologna. His research interests include nonlinear control applied to power electronics and electromechanical systems oriented to power quality enhancement, sensorless adaptive observers for electric machines, and energy-oriented optimal power/thermal management of complex computing platforms.



Davide Raggini received the Master's Degree in Automation Engineering from the University of Bologna, Italy, in 2017. He is currently holding a Research Fellow position at the Department of Electrical, Electronic and Information Engineering (DEI), at the University of Bologna, focusing on the development of embedded control systems for advanced mechatronics. His research interests include embedded real-time control systems and real-time kernels, wireless sensor networks (WSN), power and digital electrical and electronics design.



Andrea Tilli received the Ph.D. degree in system science and engineering from the University of Bologna in 2000. He is currently associate professor at the Department of Electrical, Electronic and Information Engineering "Guglielmo Marconi" (DEI) of the same university. His current research interests include applied nonlinear, adaptive and constrained control techniques, electric drives for motion control and energy generation, advanced mechatronic systems, diagnosis and prognosis of automatic machines, active power filters, and thermal control of

many-core systems-on-chip and supercomputers.